Published in final edited form as:

Biochemistry. 2019 April 02; 58(13): 1718–1727. doi:10.1021/acs.biochem.8b01309.

Differential misfolding properties of glaucoma-associated olfactomedin domains from human and mouse

Athéna C. Patterson-Orazem[1], **Shannon E. Hill**[1], **Yiming Wang**[2], **Iramofu M. Dominic**[1], **Carol K. Hall**[2], **Raquel L. Lieberman**[1]

[1]School of Chemistry & Biochemistry, Georgia Institute of Technology, Atlanta, GA 30332-0400

[2]Department of Chemical & Biomolecular Engineering, North Carolina State University, Raleigh, North Carolina 27695-7905

Abstract

Mutations in myocilin, predominantly within its olfactomedin (OLF) domain, are causative for the heritable form of open angle glaucoma in humans. Surprisingly, mice expressing Tyr423His mutant myocilin, corresponding to a severe glaucoma-causing mutation (Tyr437His) in human subjects, exhibit a weak, if any, glaucoma phenotype. To address possible protein-level discrepancies between mouse and human OLFs, which might lead to this outcome, biophysical properties of mouse OLF were characterized for comparison with those of human OLF. The 1.55 Å resolution crystal structure of mouse myocilin OLF reveals an asymmetric 5-bladed β-propeller that is nearly indistinguishable from previous structures of human OLF. Wild type and selected mutant mouse OLFs mirror thermal stabilities of their human OLF counterparts, including characteristic stabilization in the presence of calcium. Mouse OLF forms thioflavin T-positive aggregates with similar end-point morphology as human OLF, but amyloid aggregation kinetic rates of mouse OLF are faster than human OLF. Simulations and experiments support the interpretation that kinetics of mouse OLF are faster because of decreased charge repulsion arising from more neutral surface electrostatics. Taken together, phenotypic differences observed in mouse and human studies of mutant myocilin could be a function of aggregation kinetics rates, which would alter the lifetime of putatively protofibrillar intermediates.

Keywords

Crystallography; aggregation; thermal stability; amyloid; glaucoma; misfolding; kinetics

Corresponding Author Raquel L Lieberman, 901 Atlantic Drive NW, Atlanta, GA 30332-0400, 404-385-3663, 404-894-2295, raquel.lieberman@chemistry.gatech.edu.

Author Contributions

The manuscript was written through contributions of all authors. All authors have given approval to the final version of the manuscript.

ACCESSIONS

PDB code: 6NAX

Uniprot Q99972, O70624

INTRODUCTION

Mouse models offer valuable insights into human disease progression and are often the first testing grounds for novel treatments. In the case of protein misfolding disorders, however, mouse models have been somewhat less successful, either failing to replicate key disease phenotypes found in humans or exhibiting a weaker phenotype. In mouse models of tau-based Alzheimer disease and transthyretin-based amyloidosis,[1, 2] differences in observed phenotypes have been attributed to differences between the mouse and human proteins. At the molecular level, it is known that even minor changes in protein sequence can have dramatic effects on protein structure, stability, and misfolding properties in the cell.[3]

A recent addition to the list of protein misfolding disorders is a heritable sub-type of the age-onset ocular disease glaucoma, a worldwide leading cause of blindness. Mutations in human (*Homo sapiens*) myocilin (Uniprot Q99972), predominantly within its olfactomedin (*Hs*OLF) domain, are causative for glaucoma in approximately 3 million of the 70 million total glaucoma patients.[4, 5] The predominant pathogenic mechanism is a toxic gain of function: mutant myocilin is prone to cytotoxic aggregation within the trabecular meshwork (TM) cells that maintain the extracellular matrix that serves as an anatomical sieve to drain aqueous humor. This cytotoxicity hastens the causal risk factor of elevated pressure leading to retinal ganglion cell (RGC) death and vision loss characteristic of glaucoma.[6] Typically, individuals expressing a mutant form of myocilin, such as the variant Tyr437His, exhibit severely elevated intraocular pressure (IOP, 44 mmHg vs 20 mmHg in control population) at a young age (20 years old)[7, 8]. Data to date indicate that myocilin is not otherwise a susceptibility gene for sporadic forms of glaucoma[9].

Numerous glaucoma rodent models are available and widely used in the field[10], but for myocilin-associated glaucoma, a robust IOP elevation phenotype accompanied by RGC loss has been a challenge to elicit in mouse. In two mouse models that express either the human Tyr437His myocilin mutation[11] or its equivalent in *Mus musculus* myocilin (Uniprot O70624), Tyr423His[12], modest IOP elevation was measured[11, 12], but only in older mice. In these models, which both used the bacterial artificial chromosome method that overexpresses the target protein, IOP elevation was accompanied by some degenerative features in RGCs[11, 12]. No increase in IOP was observed in mice when Tyr423His was introduced in the endogenous mouse myocilin gene[13]. In a fourth transgenic model, high levels of human mutant myocilin Tyr437His expressed specifically in eye drainage structures and sclera using cytomegalovirus methods, exhibit the strongest and earliest glaucoma-like phenotypes to date[14].

Here we test the hypothesis that molecular level differences in *Hs*OLF and mouse OLF (*Mm*OLF) explain the differing phenotypes observed in these myocilin-glaucoma models. Although *Hs*OLF and *Mm*OLF share high sequence identity (87%), differences are observed in regions thought to template amyloid aggregation[15], raising the possibility this could contribute to species-based differences in disease phenotype, as in other misfolding disorders. We compare structural, biophysical, and aggregation properties of *Mm*OLF with well-studied characteristics of *Hs*OLF. Our results demonstrate high levels of similarities between the two proteins in their folded state and final aggregated states, but faster

aggregation rates observed for *Mm*OLF point to the possibility that a toxic species relevant to glaucoma is hidden in a transiently present protofibrillar intermediate.

MATERIALS AND METHODS

Molecular biology.

Codon-optimized *Mm*OLF was synthesized and sub-cloned by Genscript into pMAL-c4x vector similar to previously published *Hs*OLF, except that the Factor Xa cleavage site was replaced with a tobacco etch virus (TEV) protease cleavage site[15]. Maltose binding protein (MBP)-*Mm*OLF fusion variants Ala413Thr, Asp366Ala, Tyr423His and Ile485Phe, and MBP-*Hs*OLF variant Ile431Val/Thr435Ile were all produced by site-directed mutagenesis following manufacturer's recommended protocol (Quick-Change Lightening II Kit, Agilent) and verified by DNA sequencing (Operon or Genscript). Primer sequences are provided in Table S1.

Expression and purification.

*Hs*OLF and *Ms*OLF were purified as previously described.[16] *E. coli* Rosetta Gami 2 cells transformed with myocilin plasmid were inoculated to OD_{600} ~ 0.1 and grown in Superior Broth (US Biological) at 37 °C to OD_{600} of 0.8 to 1.0, cooled to 18 °C, then induced with 0.5 mM isopropyl-β-D-thiogalactopyranoside and 1 mM $CaCl_2$ overnight. Cells were harvested by centrifugation, flash cooled in liquid nitrogen, and stored at −80 °C. Cell paste (5 g) was gently suspended in 20 mL chilled phosphate buffered saline composed of 10 mM Na_2HPO_4/KH_2PO_4, 200 mM NaCl (PBS), supplemented with half an EDTA-free Roche Protease Inhibitor tablet and 1 mM EDTA, lysed by French press (Sim-Aminco French Press, 25 mL FA-023 cell from Thermo Electron Corporation) and centrifuged at 110,000xg (Beckman Avanti JXN3, JS-24.15 rotor). Clarified cell lysate was purified on AKTA Pure and Purifier systems (GE Healthcare) by amylose affinity chromatography (25 mL column packed with NEB Amylose Resin), equilibrated with PBS, eluted with PBS supplemented with 10 mM maltose, and concentrated in 15 mL 30 kDa-cutoff Amicon filters (Millipore) prior to fractionation by size-exclusion chromatography (SEC) with a Superdex-75 pg (GE Healthcare) in PBS buffer. For Tyr423His and Ile485Phe MBP-*Mm*OLF variants, fractions proximal to 55 mL elution volume were concentrated and further purified using a Superdex-75 GL (GE Healthcare) to eliminate residual aggregated protein. Fractions containing monomeric MBP-OLF fusion proteins were cleaved by TEV protease[17] using a 1 TEV:5 MBP-OLF mass ratio overnight at room temperature, then purified by nickel affinity (1mL HisTrap FF, GE Healthcare), amylose affinity and SEC as previously described[16]. After cleavage, pure protein was concentrated with 15-mL 10 kDa-cutoff Amicon filtration units (Millipore).

For aggregation kinetics assays, cleaved *Mm*OLF was subjected to cation-exchange after the first amylose step to bind and remove trace TEV protease. This was accomplished by diluting OLF-containing fractions to 50mM NaCl with 10 mM Na_2HPO_4/KH_2PO_4, and applying the sample to a HiTrap CaptoS column (1mL, GE Healthcare) equilibrated with 10 mM Na_2HPO_4/KH_2PO_4, 50 mM NaCl. Residual TEV protease was eluted from the column with gradient to 2M NaCl.

Protein purity was assessed by standard SDS-PAGE analysis with Coomassie staining. Protein concentrations were determined by spectrophotometry using molar extinction coefficients for fusion proteins (human: 134,775 $M^{-1}cm^{-1}$, mouse: 133,285 $M^{-1}cm^{-1}$) or for cleaved OLF (human: 68,425 M^{-1} cm^{-1} and mouse: 65,440 $M^{-1}cm^{-1}$) calculated by ExPaSy ProtParam[18]. Predicted isoelectic points were also calculated in ExPaSy.

Crystallization and structure determination.

Rectangular prismatic crystals of *Mm*OLF, 50–70 μM in diameter, grew within 3 weeks at 16 °C in 4 μL sitting drops containing 1:1 (v/v) of 30 mg/mL *Mm*OLF in PBS pH 7.2 and mother liquor solution containing 10% PEG-8000, 200 mM $MgCl_2$. Diffraction data were collected at the Southeast Regional Collaborative Access Team (SER-CAT) 22-ID beamline and processed using HKL-3000.[19] The *Mm*OLF structure was solved by molecular replacement in Phaser[20] using the *Hs*OLF structure 4WXQ as a search model. The *Mm*OLF model was iteratively built and refined using Coot[21] and Phenix.refine[20]. The structure has been deposited to the PDB with ID: 6NAX. Figures were prepared in PyMOL[22], and electrostatics using APBS-PDB_2PQR[23].

Thermal stability assay.

Thermal stability was measured by differential scanning fluorimetry using Sypro Orange (Invitrogen), as previously described[16]. Final mixtures of 30 μL were prepared at room temperature in 96-well optical plates (Applied Biosystems) and contained protein solutions at a final concentration of 0.5–1.5 μM in HEPES-buffered saline (10 mM HEPES pH 7.5, 200 mM NaCl). Where indicated, 50 mM maltose and 10 mM $CaCl_2$ were present. Each experiment contained control wells accounting for background protein, maltose and calcium fluorescence. Fluorescence data were collected on an Applied Biosciences Step-One Plus RT-PCR instrument equipped with fixed excitation wavelength (480 nm) and ROX® emission filter (610 nm). Thermal melts were performed from 25–95 °C with a 1 °C per min increase and acquired data were analyzed with Igor Pro, version 6.37 (WaveMetrics).

Thioflavin-T (ThT) endpoint fluorescence and *de novo* aggregation assays.

Aggregated MBP-*Mm*OLF species fractionated by Superdex-75 pg were concentrated to 30 μM protein and supplemented with 10 μM ThT in PBS. Aliquots (40 μL) were dispensed in triplicate in half-area flat-bottomed 96-well non-binding plates (Corning #3993). After incubation for 10 min, ThT fluorescence was measured at room temperature using excitation filter 440/30 nm and emission filter 485/20 nm (BioTek Synergy 2). Results represent the average of two biological replicates.

For *de novo* aggregation assays, which were conducted as described and validated in ref [15], triplicate samples comprising 150 μL of 30 μM cleaved, monomeric *Mm*OLF, *Hs*OLF, or *Hs*OLF variant Ile431Val/Thr435Ile and 10 uM ThT in PBS were incubated at 42 °C in black flat-bottom medium binding plates (Greiner Bio One #655076), Fluorescence was monitored over 72 hours at 10-minute intervals using the same BioTek plate reader and filters as listed above[15]. Representative results were normalized to the maximum fluorescence of wild type *Hs*OLF and plotted in Origin Professional 2016.

Coarse grain (PRIME20) molecular dynamics (cgMD) simulations.

Discontinuous molecular dynamics (DMD)[24], a fast alternative to conventional molecular dynamics, was used in conjunction with PRIME20, a coarse-grained protein model developed in the Hall group[25], to simulate the aggregation of *Mm*OLF derived peptides, which are analogous peptides to those of human peptides[26]. In the PRIME20 model, each of twenty different amino acids has three backbone spheres (NH, Cα and CO) and one sidechain sphere (R). Glycine does not have a sidechain sphere. Each sidechain sphere of the twenty different amino acids has a distinct hard sphere diameter (effective van der Waals radius) and distinct sidechain-to-backbone distances (R-Cα, R-NH, R-CO). The two major types of non-bonded interactions captured in PRIME20 are directional hydrogen bonding between backbone NH and CO spheres modeled as a directional square well potential and sidechain-sidechain square well interactions between any pair of the twenty different amino acids. Cheon *et al.*[27] used a perceptron learning algorithm to reduce the 210 possible independent square well depths between the 20 different amino acids to 19 different parameter groups while maintaining the 210 independent square well widths to ensure physically meaningful pair interaction energies in discriminating decoys from native structures in the PDB database. All the other non-bonded interactions are modeled as hard sphere interactions. A detailed description of the derivation of the geometric and energetic parameters of the PRIME20 model is given in earlier work[25, 27, 28].

DMD/PRIME20 simulations of mouse P1 and P3 peptide aggregation were performed in the canonical ensemble (fixed number of particles, constant volume and temperature). The simulation temperature was maintained constant by using the Andersen thermostat[29]. The system contained eight monomeric peptides in a cubic box with box length equal to 110.0 Å corresponding to a total peptide concentration of 20 mM. The reduced temperature was defined as $T^* = k_B T/\varepsilon_{HB}$, where the hydrogen bonding energy, ε_{HB}=12.47 kJ/mol. The reduced temperature T* was chosen to be 0.2, which corresponds to 342 K in real temperature[30]. Ten independent simulation runs were performed, each lasting for at least 220 μs.

The aggregation propensities of human and the mouse P3 were calculated by introducing the amyloid-forming propensity, β, using the following equation:

$$\beta = \frac{1}{N}\sum_{i=1}^{N}\frac{n_{HB}(i)}{n_{Site}(i)} \quad (1)$$

where $n_{HB}(i)$ is the total number of backbone hydrogen bonding sites (NH and C=O beads) on the i^{th} peptide in the aggregate that form β-sheet hydrogen bonds, and $n_{Site}(i)$ is the total number of NH and C=O beads on the i^{th} peptide in the aggregate. N is the total number of peptides in the system. β ranges from 1 for a perfect β-sheet structure with strong amyloid

forming propensity, to 0 for a monomeric state or disordered oligomer with weak amyloid forming propensity.

Atomic force microscopy (AFM).

Immediately after the ThT aggregation assay above, triplicate samples comprising 150 μL each were removed, combined into a 1.5 mL centrifuge tube, and left at room temperature overnight to pellet by gravity. After visible separation of the insoluble aggregates into a pellet, 40 μL of the pellet sample was deposited onto freshly-cleaved mica for 30 minutes, rinsed for 3 seconds with ultrapure water, and left to dry overnight in a Petri dish. After drying, the samples were imaged in air with a MFP-3D atomic force microscope (Asylum Research) using PPP-FMR (NanoAndMore) silicon tips with nominal tip radii less than 7 nm. The cantilever was driven at 60–80 kHz in alternating current mode and a scan rate of 0.5 Hz with 512 × 512-pixel or 1024 × 1024-pixel resolution. Raw image data were corrected for image bow and slope using software provided by Asylum Research.

RESULTS

*Mm*OLF structure.

To gain insight into the structural similarities and differences between native *Mm*OLF and *Hs*OLF, we solved the crystal structure of *Mm*OLF, to 1.55 Å resolution (Table 1). The 5-bladed β-propeller is nearly identical to that of *Hs*OLF (root mean squared deviation (RMSD) = 0.7 Å, Figure 1A). The disulfide clasp that covalently links the N and C termini is conserved, and the heptacoordinate Ca^{2+}, the pentacoordinate Na^{+} and corresponding coordinating ligands identified for *Hs*OLF[31] are all present and in similar conformations (Figure 1B). However, while the surface electrostatics of *Hs*OLF are predominantly negative,[31] the *Mm*OLF surface is more varied, with distinct positively-charged patches at both top and bottom faces of the propeller (Figure 1C).

Glaucoma-associated HsOLF mutations were selected as representatives for further inspection and study in the context of MmOLF, and represent a range of thermal stability[16, 32] and disease phenotype[33]. These variants range from Ala427Thr, associated with variable glaucoma phenotypes (familial and sporadic, all diagnosed past the age of 65) in a small sample[34] and which might only be causative in presence of other genetic risk factors, to the severe Tyr437His mutation which results in juvenile-onset glaucoma symptoms and dramatic elevation in IOP[8] (Figure 2A). Tyr437His and the moderate Ile499Phe variant are located within the hydrophobic interface between propeller blades, while Ala427Thr and Asp380Ala are proximal to the calcium-binding site (Figure 2A). Inspection of these positions in the context of MmOLF reinforces the similarity between the HsOLF and MmOLF structures. Tyr423 in MmOLF (due to a shorter N-terminal signal peptide in MmOLF numbering is offset from HsOLF by 14 amino acids) participates in hydrophobic packing and water-mediated beta-turn stabilizing hydrogen bonding interactions (Figure 2B), both of which are expected to be strongly impacted by mutation to histidine. Ala413 in MmOLF is located under surface loops known to be mobile in HsOLF[31] and other OLF domain family members[35], and should be able to accommodate conservative mutations (Figure 2C). Mutation of Asp366 abolishes calcium binding (Figure 2D) by

removing a key metal-coordinating side chain[31, 36]. Ile485 is engaged in hydrophobic packing, which is likely disrupted by the increased steric hindrance of mutation to phenylalanine (Figure 2E). Thus, based on structure, these mutations to MmOLF are expected to have an impact on stability and misfolding similar to that previously observed for HsOLF.

Thermal stability of wild-type and mutant *Mm*OLFs.

Expression and purification of *Mm*OLFs proceeded as for *Hs*OLF, published previously[16], utilizing a N-terminal maltose binding protein (MBP) fusion to enhance folding efficiency and as a purification handle. Similar to purification of *Hs*OLF, the initial MBP-*Mm*OLF fusion protein is isolated from *E. coli* in two forms (Figure 3A): a misfolded, thioflavin-T-positive aggregate suggestive of amyloid (Figure 3B,C) and a properly folded form used subsequently for characterization, including the structural analysis above, thermal stability and *de novo* aggregation kinetics assays below. Thermal stability of wild-type *Mm*OLF resembles that of *Hs*OLF (Table 2, Figure S1). All four disease variants (Ala413Thr, Ile485Phe, Asp366Ala, and Tyr423His) result in compromised *Mm*OLF stability, with decreases in melting temperature (ΔTm) similar to those of corresponding *Hs*OLF variants[16], albeit with slightly higher melting temperatures (Table 2). Wild-type *Mm*OLF, as well as *Mm*OLF variants Ala413Thr, Ile485Phe, and Tyr423His, were stabilized in the presence of calcium, confirming that a calcium binding site is retained as in *Hs*OLF[31, 36]. The outlier is *Mm*OLF Asp366Ala (Table 2), confirming the critical importance of Asp366 to calcium binding in *Mm*OLF, as suggested in the crystal structure (Figure 1, 2) and by analogy to its *Hs*OLF equivalent, Asp380[36].

Aggregation properties of *Mm*OLF.

Given the result of ThT-positive cellular aggregates produced by *E. coli* during expression, coupled with nearly identical thermal stabilities and native structures of *Mm*OLF and *Hs*OLF, similar *in-vitro* aggregation kinetics were expected. Surprisingly, *Mm*OLF forms ThT-positive aggregates faster than *Hs*OLF under assay conditions developed previously for *Hs*OLF, namely aggregation at 42 °C without agitation in a fluorescence plate reader[15] (Figure 4A), with statistically significant differences in ThT fluorescence ($p < 0.0001$, ANOVA) at 24 and 72 hour timepoints.

One possible explanation for the increased initial rate of *Mm*OLF aggregation includes differences in the *Mm*OLF sequence within previously-identified *Hs*OLF amyloidogenic peptide regions[15]. These amyloidogenic stretches (Figure 4B) comprise *Hs*OLF residues 326–337 (P1, *Mm*OLF residues 312–323) and residues 426–442 (P3, *Mm*OLF residues 412–428). Peptides P1 and P3 replicate disparate fibril morphologies associated with different aggregation conditions for the full *Hs*OLF domain[15]. For the experimental conditions used here, which provide high throughput *in-situ* ThT kinetic data (Figure 4A, and experimental section), aggregation is thought to be promoted by P3. We previously validated the end point aggregate formed in this non-nucleation dependent growth process as amyloid by using Congo Red absorbance, Fourier transform infrared spectroscopy, and AFM[26].

To test whether differences in aggregation propensity between *Hs*OLF and *Mm*OLF might originate in sequence differences in respective P1 (Ala to Ser) or P3 (Ile to Val, Thr to Leu) regions (Figure 4B), we first turned to coarse grain molecular modeling using DMD/PRIME20, a method we used recently to simulate aggregation of P1 and P3 peptides derived from *Hs*OLF[26]. For P1, no obvious differences were identified between mouse and human P1 aggregation simulations (Figure S2, S3), consistent with the single conservative substitution. By contrast, mouse P3 peptides, initially in random coil configurations, aggregate to form a parallel, in-register protofilament with a predominantly L-shaped backbone conformation in eight out of ten runs (Figure 4C, S4), a different shape and a more homogeneous aggregate compared to human P3, which formed a U-shaped backbone conformation in just two out of ten runs (Figure 4D)[26]. Based on the average number of inter-peptide hydrogen bonds formed per residue calculated over the last third of the simulation trajectories (Figure 4E), the two different residues, Val417 and Ile421 (corresponding to human residues Ile431 and Thr435), result in higher average β-sheet-forming propensity in the C-terminal region of the peptide and less variability than for human P3. The average β values or amyloid forming propensities for the entire peptide sequence are $\beta_{(\text{mouse P3})} = 0.52 \pm 0.05$, and $\beta_{(\text{human P3})} = 0.43 \pm 0.19$, suggesting that mouse P3 has a stronger amyloid forming propensity than human P3 (Figure 4F). These differences do not reach statistical significance ($p < 0.0985$ by normal distribution test), likely due to the heterogeneous conformational landscape of simulated human P3 aggregates, but in principle suggest variations in P3 may explain experimental differences in kinetics between *Mm*OLF and *Hs*OLF.

To experimentally evaluate whether the two amino acid differences in mouse P3 sequence account for more facile *Mm*OLF aggregation, the double *Hs*OLF variant Ile431Val/Thr435Ile was generated and subjected to an aggregation assay, in parallel with wild type *Hs*OLF and *Mm*OLF (Figure 4A). Surprisingly, aggregation kinetics were more similar to *Hs*OLF than to *Mm*OLF, indicating that the specific residues in the mouse P3 sequence are not sufficient to increase *Mm*OLF aggregation rates or increase ThT binding of the end-point aggregate. Differences between *Hs*OLF wild type and the Ile431Val/Thr435Ile variant were not statistically significant at 24 hours ($p = 0.1645$), though they were at 72 hours ($p = 0.0074$, ANOVA). From this study, we infer that other sequence differences, scattered throughout the rest of the *Mm*OLF domain, facilitate changes in the aggregation properties relative to *Hs*OLF.

Comparison of end-point aggregate morphologies of *Mm*OLF and *Hs*OLF.

Although sequence differences in P3 do not fully explain differing aggregation kinetics of *Hs*OLF and *Mm*OLF, cgMD results suggest structural differences in the aggregate at the molecular level. To determine whether these structural changes translate into a detectable morphological difference, the end-point aggregates were imaged by AFM. Both *Mm*OLF and *Hs*OLF samples show flat spherical oligomers ~ 6 nm in height and 1–2 um in diameter (Figure S5). These species are similar in height, diameter, and circular morphology to our previous results for *Hs*OLF using the same assay[15]. Still, the aggregates observed in these images are not identical. In the *Mm*OLF sample there are additional curvilinear aggregates of varying length with similar height (~6 nm) to the spherical oligomers. The background of

the *Hs*OLF is more pronounced than that of *Mm*OLF, perhaps suggesting long-lived smaller oligomeric species. Further studies, such as AFM studies at different time points during aggregation, and systematic changes to the deposition surface, would be required to delineate the statistical significance of these differences.

DISCUSSION

Myocilin-associated glaucoma resembles other amyloid diseases like Alzheimer[37] in that numerous genetic mutations lead to a similar disease phenotype[4, 5]. From other well-studied amyloid systems, we know that specific amino acid substitutions, including naturally-occurring variants across species[38, 39] and disease-associated mutations[40–42], can lead to drastic changes in amyloid morphology and structural composition relevant to the severity of disease phenotypes. On the other hand, amyloid-forming stretches with limited sequence similarity often exhibit similar aggregate structures[43], underscoring the complexity of biophysical principles underlying amyloid formation.

In the case of myocilin, non-synonymous mutations in *Hs*OLF result in a non-native protein that recruits properly folded myocilin into a template-assisted amyloid aggregation process[15, 44], leading to cell stress and death[45–48]. In vitro, modifying parameters such as elevated temperature, low pH, slow agitation, and redox manipulation also access a partially-folded state of wild-type *Hs*OLF, which in turn facilitates fibrilization[15, 44]. Other animals with with similar eye anatomy to humans[10] and mutations in the myocilin gene (*e.g.* monkey[49]) do not develop glaucoma, and robust phenotypes are not readily induced in mice[11, 13], prompting us to consider the possibility that myocilin homologs exhibit biophysical features that protect against aggregation or facilitate cellular degradation of aggregates.

Previously, the leading explanation for the weak phenotype for mouse myocilin involved a putative cytosolic peroxisomal targeting sequence unique to *Hs*OLF, proposed to be exposed only upon misfolding[50]. *Hs*OLF structures, however, reveal that the far C-terminal end of native *Hs*OLF containing the suspected obscured signal sequence extends beyond the β-propeller structural domain, in a fully solvent-accessible conformation in the native state[31], so the sequence is not hidden. Another proposed culprit for varied glaucoma phenotypes across murine myocilin glaucoma models is genetic background. Genetics are known to play an important role in eliciting a glaucoma phenotype in DBA/2J mice, which are predisposed to severe ocular-hypertension and RGC death[51]. Genetic backgrounds vary among the mice used to generate the currently available myocilin glaucoma mouse models, and could modulate phenotype severity[10, 51]. Notably, adenovirus-induced overexpression of human Tyr437His myocilin resulted in elevated IOP in A/J, BALB/cJ and C57BL/6J mice, but not in C3H/HeJ mice[52]. Finally, mutant myocilin expression levels may influence resultant phenotypes. High expression appears important for an IOP elevation phenotype in available myocilin glaucoma mouse models. TM cells, like neurons, are long-lived and highly sensitive to protein misfolding, and may not require high levels of mutant myocilin to present aberrant phenotypes, but myocilin is present at relatively high concentrations in the cellular secretion studies[53–55] as well as in our experiments. Whether mutant myocilin overexpression is a general phenotype among myocilin glaucoma patients is currently

unclear, but a recent histological analysis of a very rare sample of a glaucomatous donor eye harboring Tyr437His myocilin appears to support the finding that overexpression of mutant myocilin (relative to wild type levels in control eyes) is a factor[56].

Our characterization of *Mm*OLF structure and aggregation in this study, combined with prior cellular secretion studies demonstrating intracellular accumulation of selected mouse myocilin variants[53] to an extent similar to human disease-causing counterparts[16, 32], would predict a robust aggregation phenotype upon mutation in mouse. Namely, even though native structure and thermal stability are relatively unchanged, *Mm*OLF aggregation kinetics are faster than *Hs*OLF, which cannot be adequately explained by the two hydrophobic alterations found in the mouse P3 sequence. Increased ThT fluorescence seen for *Mm*OLF could be attributed to charge or structural differences in the aggregate species[57]. Thus, one molecular level insight from our study is that differential surface electrostatics could be altering the aggregation profile of *Mm*OLF. Compared to the largely negative *Hs*OLF surface (calculated pI 5.0), the somewhat more neutral and varied *Mm*OLF (calculated pI 5.8) is expected to exhibit faster initial aggregation, as seen in systematic studies of other model amyloid systems[58, 59]. Another molecular explanation could be the relative toxicity of the aggregates. There is an overall resemblance in endpoint morphology for *Mm*OLF and *Hs*OLF aggregates, but we know from other amyloid diseases that the intermediate aggregates are likely the neurotoxic species, not the final endpoint aggregate[60, 61]. Perhaps by aggregating more quickly, the putatively more toxic intermediate in *Mm*OLF does not have time to populate, and instead is driven to the less toxic endpoint aggregate. Since OLF is a relatively new addition to the amylome, details of such intermediates including their structure and toxicity, as well as aggregation of OLF when tethered to a coiled-coil region by a long linker[62], remain open questions. Taken together, our findings motivate further work into dissecting the factors that elicit glaucoma in mice, to further support their use in glaucoma research.

Supplementary Material

Refer to Web version on PubMed Central for supplementary material.

ACKNOWLEDGMENT

The authors acknowledge Y. Ku and Y. Ajirniar for experimental assistance, the Sulcheck laboratory for access to their AFM, and the Parker H. Petit Institute for Bioengineering (Georgia Institute of Technology) for use of core facilities equipment.

Funding Sources

This work was supported by National Institutes of Health (NIH) (R01EB006006 to C.K.H. and EYR01021205 to R.L.L.), and BrightFocus Foundation G2016027 (R.L.L). SER-CAT is supported by its member institutions, and equipment grants (S10_RR25528 and S10_RR028976) from NIH. Use of the Advanced Photon Source was supported by the U. S. Department of Energy, Office of Science, Office of Basic Energy Sciences, under Contract No. W-31–109-Eng-38.

ABBREVIATIONS

OLF	olfactomedin

Hs	Homo sapiens
Mm	Mus musculus
TM	trabecular meshwork
IOP	intraocular pressure
RGC	retinal ganglion cell
TEV	Tobacco Etch Virus
RMSD	root mean squared deviation
ThT	thioflavin-T
MBP	maltose binding protein
SEC	size exclusion chromatography
PBS	phosphate buffered saline
DMD	discontinuous molecular dynamics
ER	endoplasmic reticulum

REFERENCES

[1]. Reixach N, Foss TR, Santelli E, Pascual J, Kelly JW, and Buxbaum JN (2008) Human-murine transthyretin heterotetramers are kinetically stable and non-amyloidogenic - A lesson in the generation of transgenic models of diseases involving oligomeric proteins, J. Biol. Chem 283, 2098–2107. [PubMed: 18006495]

[2]. Ando K, Leroy K, Heraud C, Kabova A, Yilmaz Z, Authelet M, Suain V, De Decker R, and Brion JP (2010) Deletion of murine tau gene increases tau aggregation in a human mutant tau transgenic mouse model, Biochem. Soc. Trans 38, 1001–1005. [PubMed: 20658993]

[3]. Hartl FU, and Hayer-Hartl M (2009) Converging concepts of protein folding in vitro and in vivo, Nat. Struct. Mol. Biol 16, 574–581. [PubMed: 19491934]

[4]. Gong G, Kosoko-Lasaki O, Haynatzki GR, and Wilson MR (2004) Genetic dissection of myocilin glaucoma, Hum. Mol. Genet 13, R91–102. [PubMed: 14764620]

[5]. Tamm ER (2002) Myocilin and glaucoma: facts and ideas, Prog. Retin. Eye Res 21, 395–428. [PubMed: 12150989]

[6]. Stothert AR, Fontaine SN, Sabbagh JJ, and Dickey CA (2016) Targeting the ER-autophagy system in the trabecular meshwork to treat glaucoma, Exp. Eye Res 144, 38–45. [PubMed: 26302411]

[7]. Alward WL, Fingert JH, Coote MA, Johnson AT, Lerner SF, Junqua D, Durcan FJ, McCartney PJ, Mackey DA, Sheffield VC, and Stone EM (1998) Clinical features associated with mutations in the chromosome 1 open-angle glaucoma gene (GLC1A), N. Engl. J. Med 338, 1022–1027. [PubMed: 9535666]

[8]. Fingert JH, Stone EM, Sheffield VC, and Alward WL (2002) Myocilin glaucoma, Surv. Ophthalmol 47, 547–561. [PubMed: 12504739]

[9]. Wiggs JL, Allingham RR, Vollrath D, Jones KH, De La Paz M, Kern J, Patterson K, Babb VL, Del Bono EA, Broomer BW, Pericak-Vance MA, and Haines JL (1998) Prevalence of mutations in TIGR/Myocilin in patients with adult and juvenile primary open-angle glaucoma, Am. J. Hum. Genet 63, 1549–1552. [PubMed: 9792882]

[10]. Johnson TV, and Tomarev SI (2016) Animal Models of Glaucoma, In Essent Ophthalmol (Chan C, Ed.), pp 31–49, Springer International Publishing, Switzerland.

[11]. Senatorov V, Malyukova I, Fariss R, Wawrousek EF, Swaminathan S, Sharan SK, and Tomarev S (2006) Expression of mutated mouse myocilin induces open-angle glaucoma in transgenic mice, J. Neurosci 26, 11903–11914. [PubMed: 17108164]

[12]. Zhou Y, Grinchuk O, and Tomarev SI (2008) Transgenic mice expressing the Tyr437His mutant of human myocilin protein develop glaucoma, Invest. Ophthalmol. Vis. Sci 49, 1932–1939. [PubMed: 18436825]

[13]. Gould DB, Reedy M, Wilson LA, Smith RS, Johnson RL, and John SWM (2006) Mutant myocilin nonsecretion in vivo is not sufficient to cause glaucoma, Mol. Cell. Biol 26, 8427–8436. [PubMed: 16954374]

[14]. Zode GS, Kuehn MH, Nishimura DY, Searby CC, Mohan K, Grozdanic SD, Bugge K, Anderson MG, Clark AF, Stone EM, and Sheffield VC (2011) Reduction of ER stress via a chemical chaperone prevents disease phenotypes in a mouse model of primary open angle glaucoma, J. Clin. Invest 121, 3542–3553. [PubMed: 21821918]

[15]. Hill SE, Donegan RK, and Lieberman RL (2014) The glaucoma-associated olfactomedin domain of myocilin forms polymorphic fibrils that are constrained by partial unfolding and peptide sequence, J. Mol. Biol 426, 921–935. [PubMed: 24333014]

[16]. Burns JN, Orwig SD, Harris JL, Watkins JD, Vollrath D, and Lieberman RL (2010) Rescue of glaucoma-causing mutant myocilin thermal stability by chemical chaperones, ACS Chem. Biol 5, 477–487. [PubMed: 20334347]

[17]. Tropea JE, Cherry S, and Waugh DS (2009) Expression and purification of soluble His(6)-tagged TEV protease, Methods Mol. Biol 498, 297–307. [PubMed: 18988033]

[18]. Gasteiger E, Hoogland C, Gattiker A, Duvaud S, Wilkins MR, Appel RD, and Bairoch A (2005) Protein Identification and Analysis Tools on the ExPASy Server, The Proteomics Protocols Handbook, 571–607.

[19]. Minor W, Cymborowski M, Otwinowski Z, and Chruszcz M (2006) HKL-3000: the integration of data reduction and structure solution - from diffraction images to an initial model in minutes, Acta Cryst. D 62, 859–866. [PubMed: 16855301]

[20]. McCoy AJ, Grosse-Kunstleve RW, Adams PD, Winn MD, Storoni LC, and Read RJ (2007) Phaser crystallographic software, J. Appl. Cryst 40, 658–674. [PubMed: 19461840]

[21]. Emsley P, Lohkamp B, Scott WG, and Cowtan K (2010) Features and development of Coot, Acta Cryst. D 66, 486–501. [PubMed: 20383002]

[22]. Schrödinger L (2015) The PyMOL Molecular Graphics System, Version 2.0.

[23]. Jurrus E, Engel D, Star K, Monson K, Brandi J, Felberg LE, Brookes DH, Wilson L, Chen J, Liles K, Chun M, Li P, Gohara DW, Dolinsky T, Konecny R, Koes DR, Nielsen JE, Head-Gordon T, Geng W, Krasny R, Wei GW, Holst MJ, McCammon JA, and Baker NA (2018) Improvements to the APBS biomolecular solvation software suite, Protein Sci 27, 112–128. [PubMed: 28836357]

[24]. Alder BJ WT (1959) Studies in molecular dynamics I: general method, J. Chem. Phys, 459–466.

[25]. Voegler Smith A, and Hall CK (2001) Alpha-Helix Formation: discontinuous molecular dynamics on an intermediate-resolution protein model, Proteins 44, 344–360. [PubMed: 11455608]

[26]. Wang Y, Gao Y, Hill SE, Huard DJE, Tomlin MO, Lieberman RL, Paravastu AK, and Hall CK (2018) Simulations and experiments delineate amyloid fibrilization by peptides derived from glaucoma-associated myocilin, J. Phys. Chem. B 122, 5845–5850. [PubMed: 29724098]

[27]. Cheon M, Chang I, and Hall CK (2010) Extending the PRIME model for protein aggregation to all 20 amino acids, Proteins 78, 2950–2960. [PubMed: 20740494]

[28]. Nguyen HD, and Hall CK (2004) Molecular dynamics simulations of spontaneous fibril formation by random-coil peptides, Proc. Natl. Acad. Sci. U S A 101, 16180–16185. [PubMed: 15534217]

[29]. HC A (1980) Molecular dynamics simulations at constant pressure and/or temperature, J. Chem. Phys, 2384–2393.

[30]. Wang Y, Shao Q, and Hall CK (2016) N-terminal prion protein peptides (PrP(120–144)) form parallel in-register beta-sheets via multiple nucleation-dependent pathways, J. Biol. Chem 291, 22093–22105. [PubMed: 27576687]

[31]. Donegan RK, Hill SE, Freeman DM, Nguyen E, Orwig SD, Turnage KC, and Lieberman RL (2015) Structural basis for misfolding in myocilin-associated glaucoma, Hum. Mol. Genet 24, 2111–2124. [PubMed: 25524706]

[32]. Burns JN, Turnage KC, Walker CA, and Lieberman RL (2011) The stability of myocilin olfactomedin domain variants provides new insight into glaucoma as a protein misfolding disorder, Biochemistry 50, 5824–5833. [PubMed: 21612213]

[33]. Hewitt AW, Mackey DA, and Craig JE (2008) Myocilin allele-specific glaucoma phenotype database, Hum. Mutat 29, 207–211. [PubMed: 17966125]

[34]. Faucher M, Anctil JL, Rodrigue MA, Duchesne A, Bergeron D, Blondeau P, Cote G, Dubois S, Bergeron J, Arseneault R, Morissette J, Raymond V, and Quebec Glaucoma N (2002) Founder TIGR/myocilin mutations for glaucoma in the Quebec population, Hum. Mol. Genet 11, 2077–2090. [PubMed: 12189160]

[35]. Hill SE, Donegan RK, Nguyen E, Desai TM, and Lieberman RL (2015) Molecular details of olfactomedin domains provide pathway to structure-function studies, PLoS One 10, e0130888. [PubMed: 26121352]

[36]. Donegan RK, Hill SE, Turnage KC, Orwig SD, and Lieberman RL (2012) The glaucoma-associated olfactomedin domain of myocilin is a novel calcium binding protein, J. Biol. Chem 287, 43370–43377. [PubMed: 23129764]

[37]. Selkoe DJ (2001) Alzheimer's disease: genes, proteins, and therapy, Physiol. Rev 81, 741–766. [PubMed: 11274343]

[38]. Westermark P, Engstrom U, Johnson KH, Westermark GT, and Betsholtz C (1990) Islet amyloid polypeptide: pinpointing amino acid residues linked to amyloid fibril formation, Proc. Natl. Acad. Sci. U.S.A 87, 5036–5040. [PubMed: 2195544]

[39]. Theint T, Nadaud PS, Aucoin D, Helmus JJ, Pondaven SP, Surewicz K, Surewicz WK, and Jaroniec CP (2017) Species-dependent structural polymorphism of Y145Stop prion protein amyloid revealed by solid-state NMR spectroscopy, Nat. Commun 8, 753. [PubMed: 28963458]

[40]. Hatami A, Monjazeb S, Milton S, and Glabe CG (2017) Familial Alzheimer's disease mutations within the Amyloid Precursor Protein alter the aggregation and conformation of the Amyloid-beta peptide, J. Biol. Chem 292, 3172–3185. [PubMed: 28049728]

[41]. Schutz AK, Vagt T, Huber M, Ovchinnikova OY, Cadalbert R, Wall J, Guntert P, Bockmann A, Glockshuber R, and Meier BH (2015) Atomic-resolution three-dimensional structure of amyloid beta fibrils bearing the Osaka mutation, Angew. Chem. Int. Ed. Engl 54, 331–335. [PubMed: 25395337]

[42]. Ivanova MI, Sievers SA, Guenther EL, Johnson LM, Winkler DD, Galaleldeen A, Sawaya MR, Hart PJ, and Eisenberg DS (2014) Aggregation-triggering segments of SOD1 fibril formation support a common pathway for familial and sporadic ALS, Proc. Natl. Acad. Sci. U.S.A 111, 197–201. [PubMed: 24344300]

[43]. Krotee P, Griner SL, Sawaya MR, Cascio D, Rodriguez JA, Shi D, Philipp S, Murray K, Saelices L, Lee J, Seidler P, Glabe CG, Jiang L, Gonen T, and Eisenberg DS (2017) Common fibrillar spines of amyloid-beta and human Islet Amyloid Polypeptide revealed by Micro Electron Diffraction and inhibitors developed using structure-based design, J. Biol. Chem 293, 2888–2902. [PubMed: 29282295]

[44]. Orwig SD, Perry CW, Kim LY, Turnage KC, Zhang R, Vollrath D, Schmidt-Krey I, and Lieberman RL (2012) Amyloid fibril formation by the glaucoma-associated olfactomedin domain of myocilin, J. Mol. Biol 421, 242–255. [PubMed: 22197377]

[45]. Joe MK, Sohn S, Hur W, Moon Y, Choi YR, and Kee C (2003) Accumulation of mutant myocilins in ER leads to ER stress and potential cytotoxicity in human trabecular meshwork cells, Biochem. Biophys. Res. Commun 312, 592–600. [PubMed: 14680806]

[46]. Joe MK, and Tomarev SI (2010) Expression of myocilin mutants sensitizes cells to oxidative stress-induced apoptosis: implication for glaucoma pathogenesis, Am. J. Pathol 176, 2880–2890. [PubMed: 20382707]

[47]. Yam GH-F, Gaplovska-Kysela K, Zuber C, and Roth J (2007) Aggregated myocilin induces russell bodies and causes apoptosis: implications for the pathogenesis of myocilin-caused primary open-angle glaucoma, Am. J. Pathol 170, 100–109. [PubMed: 17200186]

[48]. Liu Y, and Vollrath D (2004) Reversal of mutant myocilin non-secretion and cell killing: implications for glaucoma, Hum. Mol. Genet 13, 1193–1204. [PubMed: 15069026]

[49]. Fingert JH, Clark AF, Craig JE, Alward WL, Snibson GR, McLaughlin M, Tuttle L, Mackey DA, Sheffield VC, and Stone EM (2001) Evaluation of the myocilin (MYOC) glaucoma gene in monkey and human steroid-induced ocular hypertension, Invest. Ophthalmol. Vis. Sci 42, 145–152. [PubMed: 11133859]

[50]. Shepard AR, Jacobson N, Millar JC, Pang IH, Steely HT, Searby CC, Sheffield VC, Stone EM, and Clark AF (2007) Glaucoma-causing myocilin mutants require the Peroxisomal targeting signal-1 receptor (PTS1R) to elevate intraocular pressure, Hum. Mol. Genet 16, 609–617. [PubMed: 17317787]

[51]. Johnson TV, and Tomarev SI (2010) Rodent models of glaucoma, Brain Res. Bull 81, 349–358. [PubMed: 19379796]

[52]. McDowell CM, Luan T, Zhang Z, Putliwala T, Wordinger RJ, Millar JC, John SW, Pang IH, and Clark AF (2012) Mutant human myocilin induces strain specific differences in ocular hypertension and optic nerve damage in mice, Exp. Eye Res 100, 65–72. [PubMed: 22575566]

[53]. Malyukova I, Lee HS, Fariss RN, and Tomarev SI (2006) Mutated mouse and human myocilins have similar properties and do not block general secretory pathway, Invest. Ophthalmol. Vis. Sci 47, 206–212. [PubMed: 16384964]

[54]. Vollrath D, and Liu Y (2006) Temperature sensitive secretion of mutant myocilins, Exp. Eye Res 82, 1030–1036. [PubMed: 16297911]

[55]. Gobeil S, Letartre L, and Raymond V (2006) Functional analysis of the glaucoma-causing TIGR/myocilin protein: integrity of amino-terminal coiled-coil regions and olfactomedin homology domain is essential for extracellular adhesion and secretion, Exp. Eye Res 82, 1017–1029. [PubMed: 16466712]

[56]. van der Heide CJ, Alward WLM, Flamme-Wiese M, Riker M, Syed NA, Anderson MG, Carter K, Kuehn MH, Stone EM, Mullins RF, and Fingert JH (2018) Histochemical analysis of glaucoma caused by a myocilin mutation in a human donor eye, Ophthalmol. Glaucoma 1, 132–138. [PubMed: 30906929]

[57]. Malmos KG, Blancas-Mejia LM, Weber B, Buchner J, Ramirez-Alvarado M, Naiki H, and Otzen D (2017) ThT 101: a primer on the use of thioflavin T to investigate amyloid formation, Amyloid 24, 1–16.

[58]. Chiti F, Calamai M, Taddei N, Stefani M, Ramponi G, and Dobson CM (2002) Studies of the aggregation of mutant proteins in vitro provide insights into the genetics of amyloid diseases, Proc. Natl. Acad. Sci. U S A 99 Suppl 4, 16419–16426. [PubMed: 12374855]

[59]. Hill SE, Miti T, Richmond T, and Muschol M (2011) Spatial extent of charge repulsion regulates assembly pathways for lysozyme amyloid fibrils, PLoS One 6, e18171. [PubMed: 21483680]

[60]. Hartley DM, Walsh DM, Ye CP, Diehl T, Vasquez S, Vassilev PM, Teplow DB, and Selkoe DJ (1999) Protofibrillar intermediates of amyloid beta-protein induce acute electrophysiological changes and progressive neurotoxicity in cortical neurons, J Neurosci 19, 8876–8884. [PubMed: 10516307]

[61]. Walsh DM, Hartley DM, Kusumoto Y, Fezoui Y, Condron MM, Lomakin A, Benedek GB, Selkoe DJ, and Teplow DB (1999) Amyloid beta-protein fibrillogenesis. Structure and biological activity of protofibrillar intermediates, J. Biol. Chem 274, 25945–25952. [PubMed: 10464339]

[62]. Hill SE, Nguyen E, Donegan RK, Patterson-Orazem AC, Hazel A, Gumbart JC, and Lieberman RL (2017) Structure and misfolding of the flexible tripartite coiled-coil domain of glaucoma-associated myocilin, Structure 25, 1697–1707. [PubMed: 29056483]

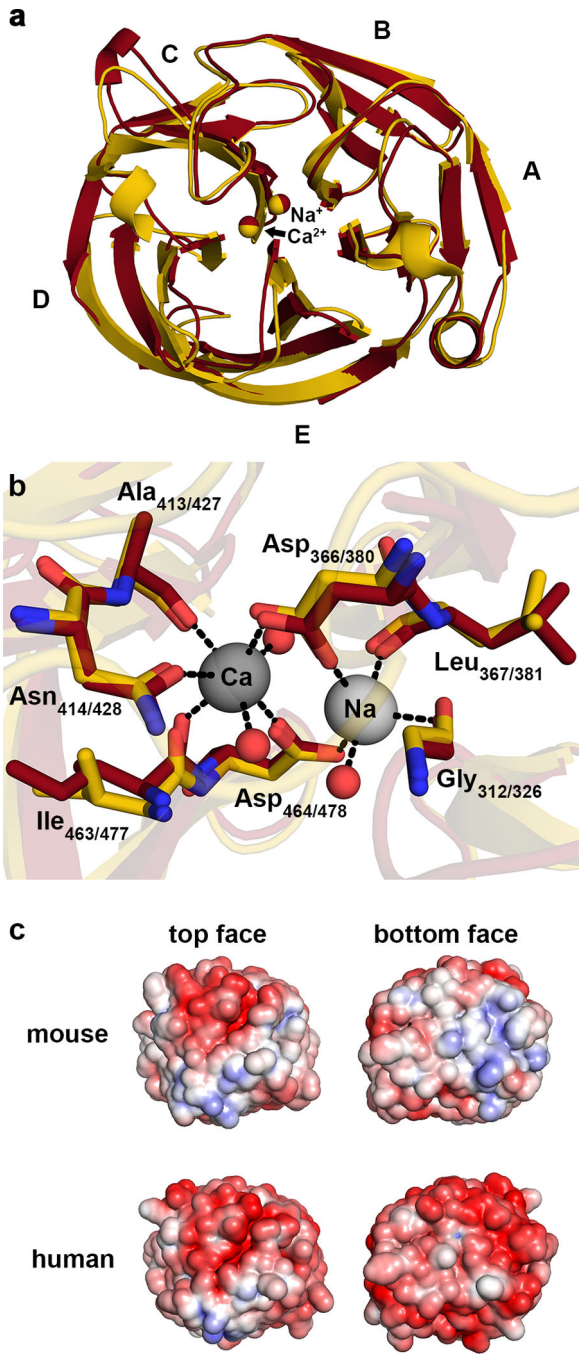

Figure 1.

*Mm*OLF and *Hs*OLF share key structural features. (A) Superposition of *Mm*OLF structure (dark red, 1.55 Å resolution) and *Hs*OLF (PDB code 4WXQ, gold, 2.15 Å resolution), view of top face, RMSD = 0.73 Å. (B) Ca^{2+}, Na^{+}, and corresponding coordinating residues in the central cavity of *Mm*OLF and *Hs*OLF are nearly identical. Waters are shown as red spheres, and hydrogen bonding interactions < 3Å are shown as dashed lines. (C) Surface electrostatics demonstrate similar potentials across the top face, but increased positive

charge on the bottom face of *Mm*OLF relative to *Hs*OLF. Surface potentials are colored negative (red, −5 kT/e-) to positive (blue, +5 kT/e-).

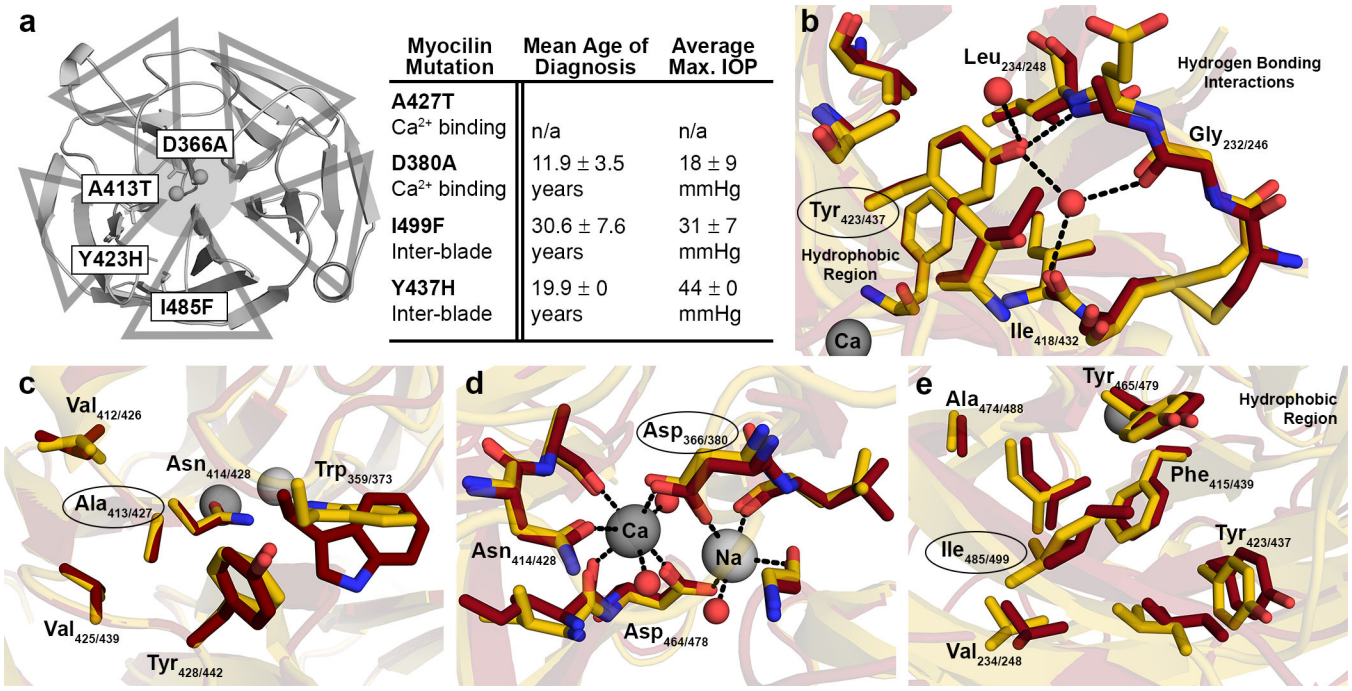

Myocilin Mutation	Mean Age of Diagnosis	Average Max. IOP
A427T Ca^{2+} binding	n/a	n/a
D380A Ca^{2+} binding	11.9 ± 3.5 years	18 ± 9 mmHg
I499F Inter-blade	30.6 ± 7.6 years	31 ± 7 mmHg
Y437H Inter-blade	19.9 ± 0 years	44 ± 0 mmHg

Figure 2.

Biochemical environment of glaucoma-causing myocilin mutations. (A) Representing a range of clinical phenotypes (table to the right)[33], select myocilin mutations are either in a hydrophobic interface between the blades, highlighted by triangles, or near the calcium-binding site, indicated by shaded circle. (B-E) Overlay of mouse, dark red, and human, gold, OLF structures demonstrate similarities in the biochemical environment of (B) human Tyr437 and its mouse equivalent Tyr423; (C) Ala427 and mouse Ala413; (D) Asp380 and mouse Asp366; and (E) Ile499 and mouse Ile485. Waters are shown as red spheres, and hydrogen bonding interactions < 3Å are shown as dashed lines.

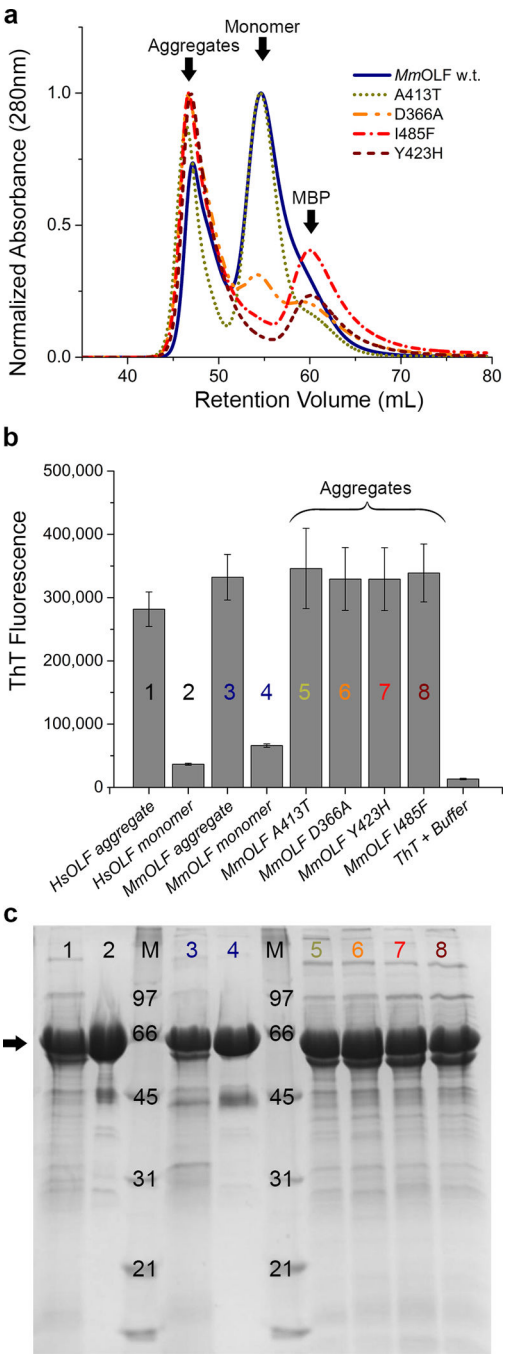

Figure 3.

Aggregates of MBP-*Mm*OLF isolated from *E. coli* are ThT-positive, a hallmark of amyloid. (A) Aligned chromatograms from Superdex-75 purifications of wild-type and mutant MBP-*Mm*OLF fusion proteins. (B) ThT fluorescence of MBP-*Mm*OLF aggregates compared to selected monomeric MBP-OLFs and (C) corresponding SDS-PAGE analysis demonstrates that, for equal amounts of protein, the average ThT fluorescence is similar for human and mouse.

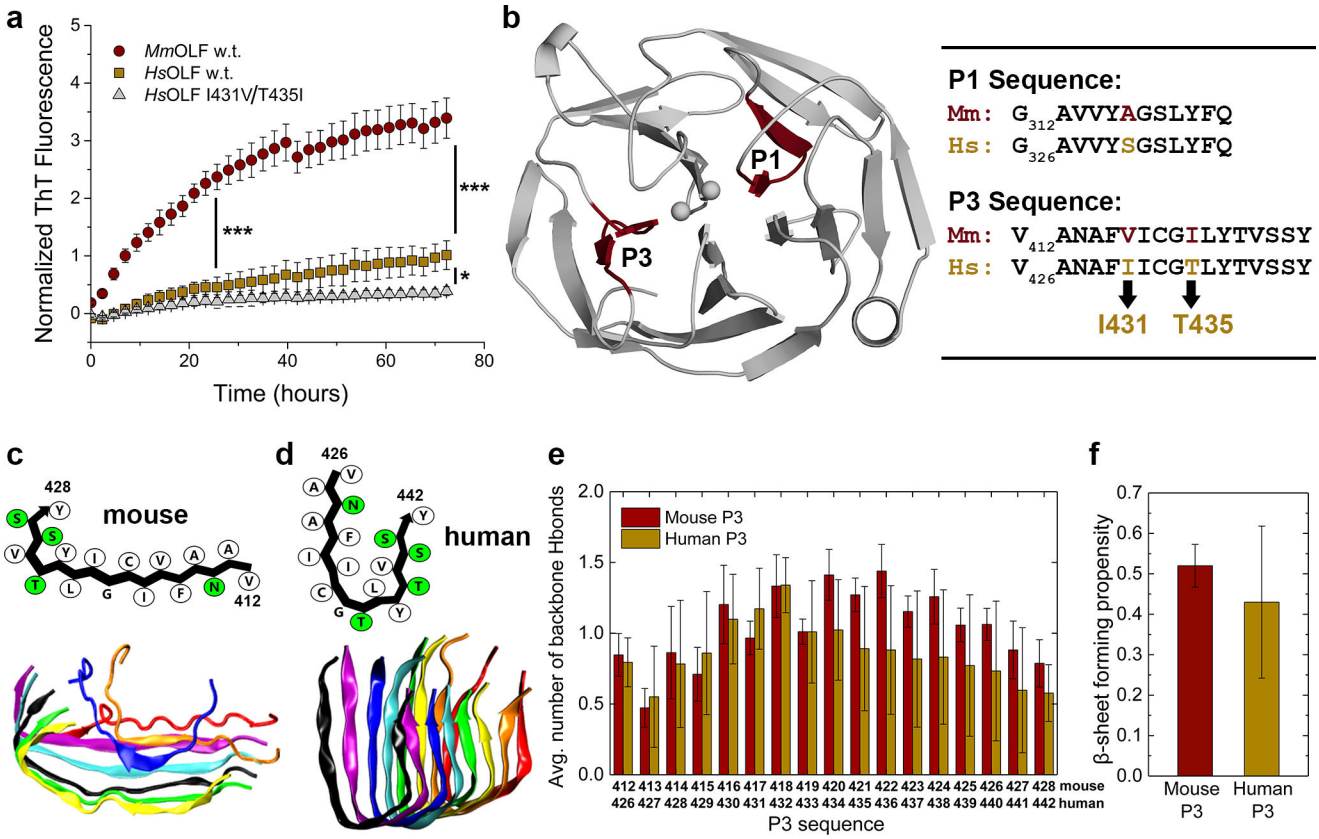

Figure 4.

*Mm*OLF aggregation kinetics, and DMD/PRIME20 simulations of amyloidogenic mouse P3. (A) Aggregation of purified *Mm*OLF, *Hs*OLF and *Hs*OLF variant I431V/T435I monitored by ThT fluorescence at 42 °C over 72 hours; * ($p < 0.01$) and *** ($p < 0.0001$) represent statistically significant differences relative to *Hs*OLF at 24h and 72h. (B) Location of amyloidogenic stretches P1 and P3 within the OLF domain (left), and sequence alignment of mouse and human P1 and P3 (right). (C) Simulated L-shaped mouse P3 protofilament in schematic representation (above) with hydrophobic and polar residues indicated in white and green, respectively, and representative final simulation snapshot (below). (D) Simulated U-shaped conformation of human P3 protofilament in schematic representation (above) and representative final simulation snapshot (below). (E) Average number of interpeptide backbone hydrogen bonds (H-bonds) formed per residue and (F) average β-sheet propensities calculated for human and mouse P3 peptides. All error bars represent standard deviation.

Table 1.

Data collection and refinement statistics for the structure of the olfactomedin (OLF) domain of mouse myocilin, PDB 6NAX.

Data Collection	
Space group	P4
Cell dimensions	
a, b, c (Å)	112.0, 112.0, 44.1
α, β, γ (degrees)	90, 90, 90
Resolution (Å)	33.11 – 1.55 (1.61 – 1.55)
Reflections	
Total	355,190 (29,541)
Unique	79,283 (7,499)
Redundancy	4.5 (3.9)
Completeness (%)	98.5 (95.2)
Wilson B-factor	11.6
R_{sym}	0.0671 (0.210)
I/Iσ	18.0 (6.1)
CC1/2	0.996 (0.950)
CC*	0.999 (0.987)
Refinement	
Resolution (Å)	33.11 – 1.55 (1.61 – 1.55)
Reflections	
Used in refinement	78,413 (7,499)
Used for R-free	2,000 (193)
R-work/R-free	0.158 (0.173) / 0.178 (0.201)
CC (work) / CC (free)	0.968 (0.934) / 0.970 (0.916)
Molecules	
Protein residues	518
Ligands	29
Solvent	623
B-factor: average	15.0
Protein residues	13.2
Ligands	26.8
Solvent	26.3
RMS	
Bond-lengths (Å)	0.01
Bond-lengths (deg)	0.88
Ramachandran	
Favored (%)	96.69
Allowed (%)	3.31
Outliers (%)	0

Data Collection	
Clashscore	3.58

Table 2.

Thermal stability of wild-type and mutant *Mm*OLF resemble *Hs*OLF counterparts. Melting temperature (T_M) measured by differential scanning fluorimetry.

Protein	Mouse		Human	
	T_M (°C)	ΔT_M + $CaCl_2$	T_M (°C)	ΔT_M + $CaCl_2$
Wild Type	52.3 ± 0.1	+ 7.8	53.0 ± 0.5	+ 6.6
A413T (A427T[a])[b]	50.8 ± 0.1	+ 8.1	48.3 ± 0.3	+ 6.9
D366A (D380A)[b]	47.5 ± 0.2	− 1.2	46.6 ± 0.3	− 1.5
I485F (I499F)[b]	43.9 ± 0.5	+ 8.5	42.8 ± 0.1	+ 7.6
Y423H (Y437H)[b]	42.1 ± 0.1	+ 9.8	40.3 ± 0.4	+ 8.3
(I431V/T435I)[c]	n/a	n/a	54 ± 2	+8.8

[a] Numbering for *Hs*OLF mutants shown in parentheses.

[b] Literature values[36] listed.

[c] Values obtained using cleaved *Hs*OLF.